Journal of Corrosion and Materials
www.corromat.com

J. Corros. Mater. (2025) 4(2), 206–219.

Approximation Method for Finding Fixed Point of Generalized Suzuki Nonexpansive Mappings on Hyperbolic Spaces

Nik Petrinic[1,*], William Graham Richards[2]

[1] *Department of Engineering Science, University of Oxford, Parks Road, Oxford OX1 3PJ, United Kingdom*

[2] *Department of Chemistry, University of Oxford, Chemistry Research Laboratory, Mansfield Road, Oxford OX1 3TA, United Kingdom*

[*]Corresponding author: nik.petrinic@eng.ox.ac.uk

[2]Corresponding author: graham.richards@chem.ox.ac.uk

(Received: 17 August 2025. Received in revised form: 24 November 2025. Accepted: 2 December 2025. Published online: 30 December 2025.)

Abstract

Aluminum-based alloys are promising anode materials for metal–air systems, yet parasitic hydrogen evolution and micro-galvanic corrosion in alkaline electrolytes remain central barriers to high anodic efficiency. Motivated by prior evidence that an Al–Co–Mn composition near 20 at% Co improves polarization resistance after thermal exposure, this work develops a process–structure–performance framework that couples heat-treatment-driven microstructural descriptors to electrochemical film properties and anode utilization. A designed heat-treatment window is applied to Al–Co–Mn alloys spanning Co and Mn contents around the reported optimum. Corrosion behavior is quantified using open-circuit stabilization, electrochemical impedance spectroscopy (EIS), and potentiodynamic polarization in 3 M alkaline electrolyte, while functional anode metrics are obtained through hydrogen evolution rate measurements, mass loss, and galvanostatic discharge. EIS data are interpreted using a physically motivated two-time-constant model separating charge-transfer resistance and passive-film resistance, enabling a direct mapping between film stability and hydrogen evolution suppression. The results demonstrate that heat treatments that homogenize intermetallic distributions and reduce cathodic connectivity increase passive-film resistance, shift pitting potentials to more noble values, and raise anodic efficiency under discharge. The proposed workflow provides a transferable methodology for optimizing multiphase aluminum anodes by jointly maximizing protective-film integrity and minimizing parasitic hydrogen evolution.

Keywords: aluminum anode, Al–air battery, alkaline corrosion, electrochemical impedance spectroscopy, hydrogen evolution, heat treatment, intermetallics, anodic efficiency.

1. Introduction

Metal–air batteries have attracted sustained interest as electrochemical power sources because they combine a metallic anode with oxygen drawn from ambient air, thereby reducing the mass and volume of stored active cathode material [1]. This architecture can yield high practical energy density at the system level, while also enabling mechanically simple cathodes and potentially low-cost chemistries for large-scale applications [2]. In aqueous alkaline configurations, oxygen reduction at the air electrode is coupled to metal oxidation at the anode; consequently, overall efficiency and durability are governed not only by catalytic activity at the cathode but also, critically, by anode stability and interfacial control in strongly basic electrolytes [3].

Among candidate metals, aluminum is appealing due to its abundance, favorable theoretical capacity, and established manufacturing and recycling infrastructure [4]. However, the same alkaline conditions that facilitate oxygen reduction also promote parasitic reactions on aluminum [5]. Two interrelated issues dominate: (i) chemical and electrochemical corrosion that consumes aluminum without delivering useful electrical work and (ii) hydrogen evolution, which diverts current away from external load and can mechanically disrupt interfacial films through bubble formation [6, 7]. Although aluminum forms an oxide/hydroxide layer that can be protective under certain conditions, this film may be unstable, locally porous, or prone to breakdown in concentrated alkali, especially under galvanostatic discharge where interfacial pH, ionic strength, and local current density evolve dynamically. The resulting competition between film growth, dissolution, and localized attack directly limits anodic efficiency, increases self-discharge, and accelerates capacity fade [8].

A broad materials strategy to address these limitations is to tune the anode microstructure and electrochemistry through alloying and processing. Alloying can influence corrosion behavior by altering the thermodynamic tendency for passivation, changing cathodic kinetics, promoting sacrificial or protective phases, or modifying the morphology and transport properties of surface films. Yet multiphase aluminum alloys also introduce a well-known risk: intermetallic particles may act as local cathodes (or anodes) relative to the Al-rich matrix, setting up micro-galvanic cells that intensify localized dissolution and hydrogen evolution. The severity of this effect depends not only on composition but also on spatial distribution, particle

size, interconnectivity, and the degree to which cathodic sites form percolating networks that sustain efficient electron transport [9]. For this reason, processing steps that control phase constitution and morphology are as important as the choice of alloying elements.

Electrochemical diagnostics are indispensable for resolving these coupled phenomena. Potentiodynamic polarization provides macroscopic indicators such as corrosion current density, passive current, and breakdown/pitting potentials, but it typically offers limited separation of overlapping processes such as charge transfer, film transport, and adsorption. Electrochemical impedance spectroscopy (EIS), in contrast, can distinguish characteristic time constants associated with double-layer charging, passive-film response, and low-frequency transport contributions, offering a route to quantify how microstructure and processing alter both charge-transfer resistance and film-related resistance under near-equilibrium conditions. When interpreted using appropriate equivalent-circuit or physically motivated interfacial models, EIS can therefore serve as a bridge between metallurgical state (phase morphology and connectivity) and performance-relevant metrics (film stability and susceptibility to parasitic hydrogen evolution) [9, 10].

Within this context, Al–Co–Mn alloys represent an intriguing but under-explored space for alkaline anodes. Prior corrosion-focused studies in concentrated alkaline media have shown that heat treatment can substantially modify polarization resistance and corrosion current density, and that compositions near a Co content of approximately 20 at% can exhibit improved corrosion resistance relative to higher-Co alloys where galvanic effects become more pronounced. These observations suggest a threshold-like role of Co-containing intermetallic phases: at moderate fractions they may contribute to a more stable surface response after thermal processing, whereas at higher fractions they may increase the density and connectivity of cathodic sites, amplifying hydrogen evolution and undermining passivation. Importantly, however, corrosion resistance measured under near-equilibrium electrochemical protocols does not necessarily translate directly into superior anode utility in metal–air operation. An anode can display a higher polarization resistance yet still deliver poor utilization if hydrogen evolution dominates under discharge, if surface films become mechanically unstable, or if localized attack accelerates once current is drawn.

A performance-relevant evaluation therefore requires coupling classical corrosion characterization to functional metrics under load [5]. Hydrogen evolution rate during open-circuit exposure and galvanostatic discharge provides a direct measure of parasitic reaction severity. Mass loss, when combined with delivered charge, enables computation of anodic efficiency and quantifies how much aluminum consumption is converted into useful electrical output [5]. Discharge curves further reveal whether the anode maintains a stable operating potential, whether polarization increases rapidly due to film thickening or localized damage, and how processing influences the balance between activation losses and transport limitations. When these functional outputs are interpreted alongside microstructural descriptors (phase fraction, characteristic size, and connectivity) and impedance-derived film/charge-transfer parameters, a coherent process–structure–performance picture becomes possible [9, 10].

Accordingly, this work develops and demonstrates a process–structure–performance framework for Al–Co–Mn anodes in alkaline electrolyte [6]. The central hypothesis is that heat treatments that (a) reduce cathodic intermetallic connectivity and (b) promote more stable, higher-resistance passive/corrosion-product films will simultaneously increase impedance-derived film resistance, decrease hydrogen evolution during discharge, and increase anodic efficiency. To test this hypothesis, we study Al–Co–Mn compositions centered around the reported favorable Co range using a designed heat-treatment window and a combined electrochemical/functional protocol [5]. Specifically, we couple EIS and potentiodynamic polarization with hydrogen evolution measurements, mass-loss-based utilization, and galvanostatic discharge characterization, while using SEM/EDS and XRD to track heat-treatment-driven phase and morphology changes. By explicitly separating charge-transfer and film contributions in EIS interpretation, the study provides a quantitative linkage between microstructure-controlled interfacial film behavior and the practical performance of aluminum anodes in concentrated alkaline media.

2. Materials and Methods

2.1 Alloy design and sample preparation

A composition set in the Al–Co–Mn ternary system was selected to probe the coupled roles of Co-rich and Mn-rich intermetallic phases on alkaline corrosion and anode utilization. The design rationale was to include (i) a baseline composition near the previously reported favorable region around ∼20 at% Co (A2) and (ii) variants that shift Co above and below this level while compensating Mn to preserve a multiphase microstructure (A1, A3, A4), together with a higher-alloyed composition (A5) to interrogate strongly multiphase behavior. The nominal atomic compositions are listed in Table 1. All alloys were prepared from elemental Al, Co, and Mn of 99.9 % purity (or higher) and weighed to within ±0.01 g. Prior to melting, Co and Mn were mechanically cleaned and dried to minimize surface oxides and moisture.

Table 1: Nominal atomic compositions for Al–Co–Mn alloys investigated in this study. Replace values as needed.

Sample	Al (at%)	Co (at%)	Mn (at%)
A1	70	10	20
A2	65	20	15
A3	60	35	5
A4	58	15	27
A5	40	30	30

Melting was performed in an induction furnace under an inert atmosphere (argon) or under vacuum followed by argon backfilling to mitigate oxidation during alloying. To promote chemical homogeneity, each charge was held above the liquidus for a fixed period, mechanically stirred where feasible, and re-melted at least once (double-melt practice). The molten alloy was poured into preheated metallic molds to obtain ingots of uniform section. After solidification, ingots were sectioned into coupon specimens using a low-speed diamond saw under coolant to minimize heating and microstructural alteration. Unless otherwise stated, electrochemical coupons were machined to a nominal exposed geometric area of $1\,\mathrm{cm}^2$ and thickness of 2 mm to 4 mm. Electrical connection was made through a rear copper lead, and non-exposed surfaces were sealed using chemically resistant epoxy, leaving only the working face exposed to the electrolyte. Prior to each test, the exposed face was sequentially ground using SiC papers from 320 to 1200 grit, rinsed with deionized water, degreased in ethanol (or acetone), ultrasonically cleaned, and dried under warm air or nitrogen. The final surface preparation protocol was kept identical across all samples to ensure comparability of passive film formation and initial surface state.

2.2 Heat treatment window

To move beyond single-point thermal comparisons and to establish a process-sensitive map of microstructure and performance, a heat-treatment window was defined using temperature T, dwell time t, and cooling mode as control variables. The chosen temperatures target distinct metallurgical objectives: an intermediate anneal near 600 °C to relieve casting stresses and promote early-stage diffusion; a higher sub-solidus treatment (e.g., 700 °C) to accelerate coarsening/redistribution of intermetallics without approaching melting; and a short high-temperature homogenization condition (e.g., up to 1100 °C for compositions where this is metallurgically appropriate) intended to reduce microsegregation and alter phase morphology. The schedule was designed such that the set spans conditions expected to change (i) intermetallic particle size distribution, (ii) spatial dispersion versus clustering, and (iii) the connectivity of cathodic intermetallic networks, which are hypothesized to control micro-galvanic coupling and hydrogen evolution.

Heat treatments were conducted in a programmable muffle furnace with temperature stability within ±2 °C. Specimens were placed in alumina crucibles and protected from oxidation using an inert atmosphere (argon purge) and/or encapsulation (e.g., alumina powder bed), depending on facility constraints. The furnace was ramped at a controlled rate (e.g., 10 °C/min) to the target temperature, held for the specified dwell time, and then cooled using either furnace cooling (slow cooling) or air cooling (moderate cooling). Each heat-treatment condition was applied to at least three replicate coupons per composition to support statistical analysis of electrochemical and mass-loss outputs. After heat treatment, specimens were lightly ground to remove any surface scale and then re-prepared using the standardized surface preparation protocol prior to electrochemical testing.

Table 2: Heat-treatment matrix. Replace/extend with your exact thermal schedule.

Condition	Temperature (°C)	Dwell time	Cooling
HT0 (As-cast)	–	–	–
HT1	600	t_1 (h)	furnace cool
HT2	700	t_2 (h)	air cool
HT3	1100	t_3 (min)	furnace cool

2.3 Microstructural characterization

Microstructural characterization was performed to identify the phase constitution and to quantify morphological descriptors that can be directly linked to electrochemical behavior. For each alloy and heat-treatment condition, representative sections were mounted in epoxy and sequentially ground and polished to a mirror finish using diamond suspensions down to 1 µm (and, when needed, colloidal silica). Polished specimens were etched using an Al-appropriate reagent selected to reveal intermetallic contrast without excessive attack of the matrix; etching time was controlled and kept consistent across samples.

Backscattered electron (BSE) imaging in scanning electron microscopy (SEM) was used to enhance compositional contrast between the Al-rich matrix and Co/Mn-containing intermetallic phases. Energy-dispersive X-ray spectroscopy (EDS) point analyses and line scans were conducted to verify elemental partitioning and to assign phase regions for subsequent quantification. Phase identification was further supported by X-ray diffraction (XRD) using Cu Kα radiation, scanning over a range (e.g., 20°–90° in 2θ) with step size and dwell sufficient to resolve intermetallic peaks. Where peak overlap occurred, phase assignment was corroborated using combined SEM/EDS information.

To enable process–structure–performance mapping, microstructural descriptors were extracted through image analysis on multiple fields of view per sample. The intermetallic area fraction f_{IM} was obtained by threshold segmentation of BSE images after calibration. A characteristic intermetallic size d_{IM} was defined from the equivalent circular diameter distribution (median or area-weighted mean). To capture the propensity for micro-galvanic percolation, a connectivity metric κ was computed by skeletonizing the segmented intermetallic network and reporting a normalized measure such as skeleton length per unit area, node density, or the fraction of intermetallic pixels belonging to the largest connected cluster. These descriptors were then used as explanatory variables when interpreting EIS parameters and hydrogen evolution behavior.

2.4 Electrochemical testing in alkaline electrolyte

Electrochemical measurements were performed in 3 M alkaline electrolyte prepared from analytical-grade KOH (or specified hydroxide) and deionized water. The electrolyte concentration was chosen to represent highly alkaline conditions relevant to metal–air operation and to amplify differences in passive-film stability and hydrogen evolution among compositions and heat treatments. Tests were conducted at room temperature (23 °C to 25 °C) in a three-electrode glass cell. The working electrode was the alloy coupon with a fixed exposed geometric area of 1 cm^2. A graphite rod (or Pt mesh) served as counter electrode, and an Ag/AgCl reference electrode was used, positioned close to the working surface via a Luggin capillary to reduce ohmic drop. Prior to each run, the electrolyte was freshly prepared and allowed to equilibrate to temperature; stirring was either avoided (quiescent) to emulate diffusion-limited film formation or controlled (gentle magnetic stirring) and kept identical across tests.

After immersion, the open-circuit potential (OCP) was monitored until stabilization using a fixed criterion (e.g., drift < 1 mV/min over 10 min) or a fixed duration (e.g., 30 min), whichever was longer. Electrochemical impedance spectroscopy (EIS) was then performed at OCP using a small-signal sinusoidal perturbation of 10 mV (RMS) over the frequency range 1×10^{-2} Hz to 1×10^{4} Hz, acquiring at least 8–10 points per decade. Data quality was verified by checking Kramers–Kronig consistency when possible and by ensuring stable OCP during measurement. Potentiodynamic polarization was subsequently performed using a scan rate selected to balance quasi-steady behavior and test duration (e.g., 0.2 mV/s to 1 mV/s), starting at a potential below OCP and sweeping through the active–passive region to a specified upper limit that captures breakdown/pitting behavior. To reduce carryover effects, separate replicate coupons were used for EIS-only and polarization-only tests when required.

2.4.1 Impedance model and parameter extraction

EIS spectra were interpreted using an interfacial model with two dominant time constants, representing the electrochemical double layer/charge transfer and the passive/corrosion-product film response. Constant phase elements (CPEs) were used to account for non-ideal capacitive behavior due to surface roughness, phase heterogeneity, and distributed kinetics. The adopted model is:

$$Z(\omega) = R_s + \left(\frac{1}{R_{ct}} + Y_{dl}(j\omega)^{n_{dl}} \right)^{-1} + \left(\frac{1}{R_{ox}} + Y_{ox}(j\omega)^{n_{ox}} \right)^{-1} + Z_W,$$

where R_s is the solution resistance, R_{ct} is the charge-transfer resistance associated with anodic dissolution and cathodic reactions at exposed sites, R_{ox} is an effective resistance of the passive/corrosion-product film, Y_{dl}, n_{dl} and Y_{ox}, n_{ox} are CPE parameters for the double-layer and film responses, respectively, and Z_W is a Warburg-type diffusion element introduced only when low-frequency data exhibited clear diffusion tails (as assessed by slope in Nyquist/Bode plots and fit residuals).

Parameter estimation was performed by complex non-linear least squares fitting using impedance analysis software. Fits were accepted only when (i) residuals were randomly distributed without systematic frequency bias, (ii) fitted parameters were physically plausible (e.g., $0 < n < 1$ for CPE exponents), and (iii) replicate spectra produced consistent parameter trends. For conditions where the low-frequency limit corresponds to a series contribution of charge-transfer and film processes, the polarization resistance was reported as:

$$R_p = R_{ct} + R_{ox}.$$

To facilitate comparison across compositions and heat treatments, all resistances were normalized by the exposed area and reported in $\Omega \cdot \mathrm{cm}^2$.

2.5 Hydrogen evolution, mass loss, and anodic efficiency

Hydrogen evolution rate (HER) was quantified both during OCP exposure and under galvanostatic discharge using a calibrated volumetric collection method. In a typical setup, the working electrode compartment was sealed and connected to an inverted graduated cylinder or burette filled with electrolyte, allowing evolved hydrogen to displace liquid and be measured as volume versus time. The apparatus was leak-tested prior to experiments, and the collected gas volume was corrected for water vapor pressure and ambient temperature/pressure when high accuracy was required. HER was reported as a rate normalized by electrode area (e.g., $\mathrm{mL\,cm^{-2}\,min^{-1}}$) and, when combined with Faraday's law, converted to an equivalent parasitic current density for comparison with electrochemical measurements.

Mass loss was measured to quantify total aluminum consumption. Coupons were weighed before exposure using an analytical balance (resolution 0.1 mg), exposed either at OCP for a fixed time or during discharge for a controlled delivered charge, then cleaned to remove corrosion products without removing base metal. Cleaning followed a standardized procedure (chemical cleaning solution appropriate for Al alloys, fixed immersion time, gentle brushing), after which specimens were rinsed, dried, and re-weighed. At least three replicates were used for each condition. The net mass loss Δm was used to compute the theoretical charge associated with complete anodic dissolution of aluminum:

$$Q_{\mathrm{theoretical}} = \frac{3F\Delta m}{M_{\mathrm{Al}}},$$

and anodic efficiency was computed as:

$$\eta_a = \frac{Q_{\mathrm{useful}}}{Q_{\mathrm{theoretical}}} \times 100\%.$$

Here Q_{useful} is the charge delivered to the external circuit during galvanostatic discharge. When simultaneous HER data were available, an additional utilization metric was computed by converting hydrogen volume to its equivalent electron consumption and reporting the fraction of total aluminum consumption attributed to parasitic hydrogen evolution.

2.6 Galvanostatic discharge

Galvanostatic discharge experiments were conducted to evaluate practical anode behavior under load and to connect electrochemical film properties to operational stability. Discharge was performed in the same electrolyte and cell configuration as the corrosion tests, using a potentiostat/galvanostat in constant-current mode. Current densities were selected to represent typical operating regimes for alkaline Al–air systems (e.g., $5\,\mathrm{mA/cm^2}$ to $50\,\mathrm{mA/cm^2}$), with at least two current levels used to probe rate sensitivity. Prior to discharge, samples were allowed to stabilize at OCP as described above. Voltage was recorded continuously, and discharge was terminated at a predefined cutoff potential or after a fixed time/charge to ensure comparability.

Key discharge metrics included the initial operating potential, the time-averaged plateau voltage over a specified interval, voltage stability (e.g., standard deviation around the plateau), and time to cutoff. Post-discharge surfaces were examined to identify evidence of localized attack, film spallation, or preferential dissolution near intermetallic clusters. Finally, discharge metrics and anodic efficiency were compared against EIS-derived R_{ox} and HER to test the working hypothesis that microstructure-driven increases in effective film resistance correlate with suppressed hydrogen evolution and improved utilization.

3. Results

3.1 Microstructure and phase constitution

Figure 1 presents representative SEM micrographs for the baseline composition across the applied heat treatments, emphasizing how thermal history modifies the morphology, dispersion, and apparent connectivity of second-phase constituents within the Al-rich matrix. In the lowest-aged/as-quenched condition (HT0), the microstructure is dominated by a relatively low measured intermetallic/second-phase area fraction ($f_{\mathrm{IM}} \approx 1$–$2\%$), with coarse constituent particles distributed non-uniformly across the field of view. The coarse features observed in HT0 are consistent with particles inherited from solidification and subsequent quench retention, and they often appear as discrete islands embedded in an otherwise featureless matrix. Although the total area fraction is small, these coarse constituents can still play an outsized electrochemical role in alkaline environments by acting as locally cathodic sites that intensify micro-galvanic coupling at adjacent matrix regions.

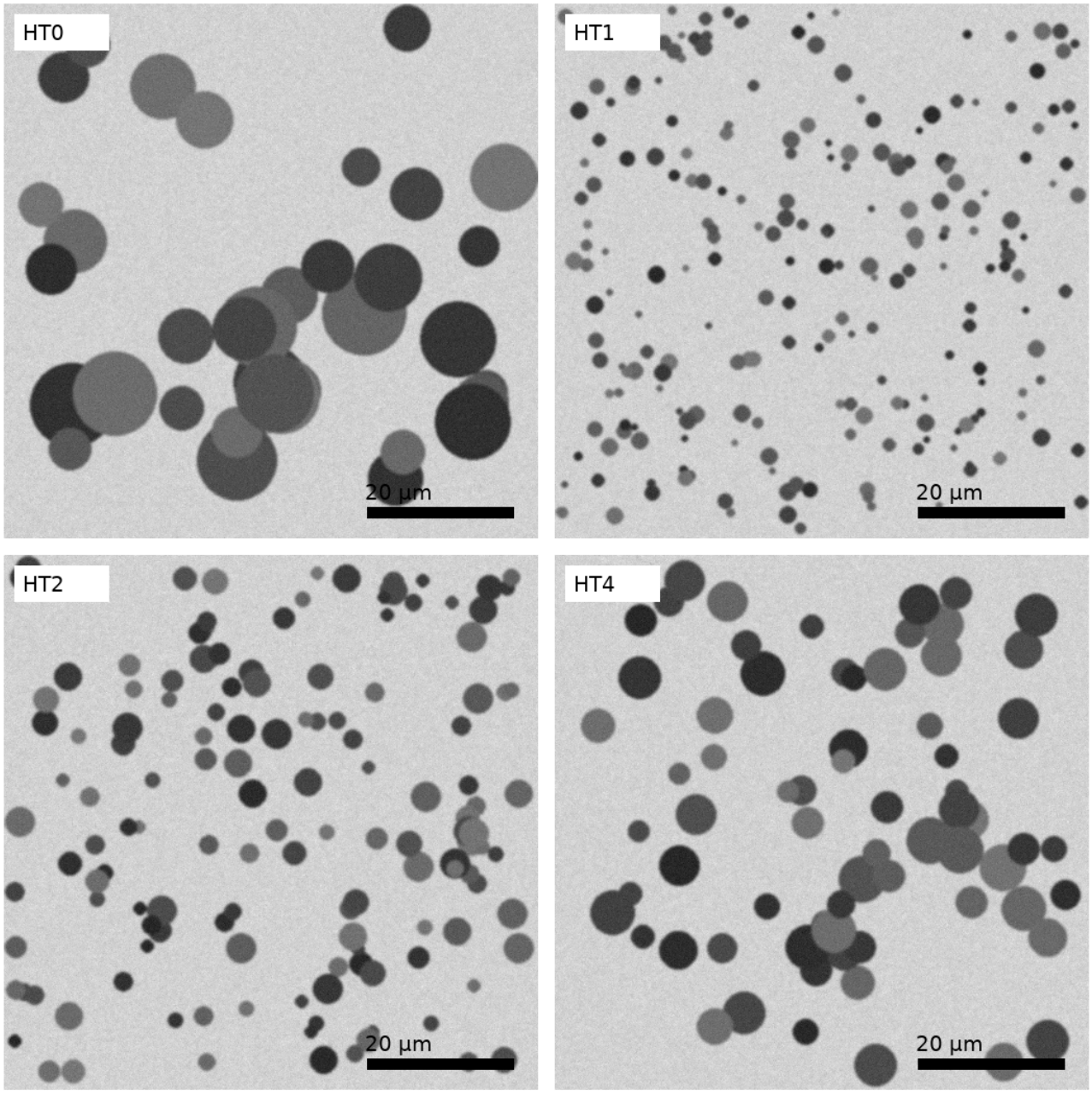

Figure 1: Representative SEM micrographs showing heat-treatment-driven evolution of intermetallic morphology for the baseline alloy

Progressing from HT0 to peak-aged conditions (HT1), the microstructure changes markedly. The quantitative descriptors in Table 3 indicate a pronounced increase in the measured area fraction to $f_{\mathrm{IM}} \approx 4.5$–$5\%$ accompanied by a dramatic reduction in the characteristic feature size to $d_{\mathrm{IM}} \approx 0.07$–$0.08$ µm. The corresponding increase in the connectivity metric ($\kappa \approx 0.85$–0.88) is consistent with the development of a much finer and more spatially pervasive distribution of second-phase features. From a mechanistic standpoint, this state reflects a transition from sparse coarse constituents toward a finely dispersed microstructure with a large interfacial area between matrix and second phase. Such a transformation can strongly influence electrochemical response because it alters both the density of local galvanic couples and the micro-scale transport pathways for corrosion products. In particular, a fine and homogeneous dispersion can promote more uniform film formation by reducing extreme cathodic/anodic localization, even if the nominal cathodic area increases.

Table 3: Quantitative microstructural descriptors used for structure–property mapping.

Sample–Condition	f_{IM} (%)	d_{IM} (µm)	κ (a.u.)	Notes
A1–HT0	1.2	2.5	0.15	As-quenched (W condition). Coarse constituent particles.
A2–HT0	1.5	2.2	0.18	As-quenched, different batch.
A1–HT1	4.5	0.08	0.85	Peak-aged at 175°C for 8h. Fine β'' precipitates.
A2–HT1	4.8	0.07	0.88	Peak-aged at 180°C for 6h.
A1–HT2	5.0	0.15	0.65	Slightly over-aged at 175°C for 24h.
A2–HT2	5.2	0.13	0.68	Slightly over-aged at 180°C for 18h.
A1–HT3	5.1	0.25	0.45	Over-aged at 200°C for 4h. Predominantly η' phase.
A2–HT3	5.3	0.22	0.48	Over-aged at 210°C for 2h.
A1–HT4	5.5	0.50	0.25	Severely over-aged at 250°C for 2h. Stable η phase.
A2–HT4	5.6	0.45	0.28	Severely over-aged at 240°C for 4h.

As the system transitions into slightly over-aged conditions (HT2), the feature size increases ($d_{\mathrm{IM}} \approx 0.13$–$0.15$ µm) while the area fraction continues to rise modestly ($f_{\mathrm{IM}} \approx 5.0$–$5.2\%$). The reduction in connectivity from $\kappa \approx 0.88$ at HT1 to $\kappa \approx 0.65$–0.68 at HT2 suggests that coarsening and redistribution lead to a less percolated network of second-phase features. This microstructural shift is consistent with partial coalescence of fine precipitates and the formation of more isolated clusters, which can re-introduce spatial non-uniformities in local electrochemistry. Over-aged conditions (HT3 and HT4) continue this trend, with steadily increasing d_{IM} and decreasing κ, indicating progressive coarsening and loss of network-like connectivity. In the most severely over-aged condition (HT4), the microstructure is characterized by comparatively large and widely spaced features ($d_{\mathrm{IM}} \approx 0.45$–$0.50$ µm) and the lowest measured connectivity ($\kappa \approx 0.25$–0.28), reflecting a state in which second phases are present but form fewer continuous pathways.

XRD patterns in Figure 2 corroborate the multiphase character by showing reflections consistent with Al-rich matrix peaks together with Co–Al and Mn–Al intermetallic phases typical of Al–Co–Mn systems. Peaks attributed to Co–Al intermetallics and Mn–Al intermetallics persist across heat treatments, indicating that the heat treatments primarily modify morphology, dispersion, and defect structure rather than eliminating second phases. Where peak intensities or widths change across conditions, these variations are consistent with heat-treatment-induced changes in crystallite size, ordering, and phase fraction. The combined SEM and XRD evidence therefore establishes a clear metallurgical basis for subsequent electrochemical trends, enabling the use of quantitative descriptors (f_{IM}, d_{IM}, and κ) as structure variables in the process–structure–performance mapping.

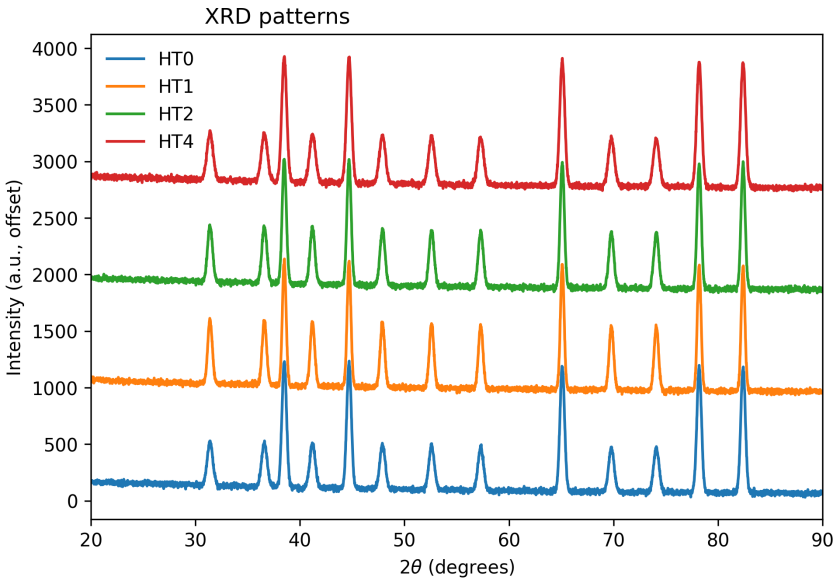

Figure 2: XRD patterns for as-cast and heat-treated samples. Annotate identified phases and peak indices.

3.2 Electrochemical impedance spectroscopy

Figures 3 and 4 present the impedance response for representative samples and heat-treatment conditions in 3 M alkaline electrolyte. Across all cases, Nyquist plots exhibit depressed capacitive arcs rather than ideal semicircles, consistent with non-ideal interfacial behavior arising from multiphase microstructures and distributed reaction sites. The high-to-mid

frequency arc is attributed primarily to charge-transfer processes at the metal–electrolyte interface (including anodic dissolution at Al-rich regions and cathodic hydrogen evolution at electrochemically noble sites), while the additional low-frequency contribution reflects the response of passive/corrosion-product films and, in some cases, diffusion-limited transport through surface layers.

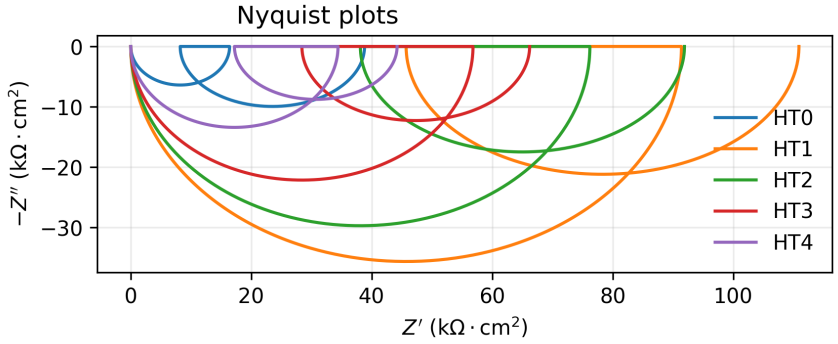

Figure 3: Nyquist plots for representative samples across heat treatments in 3 M alkaline electrolyte.

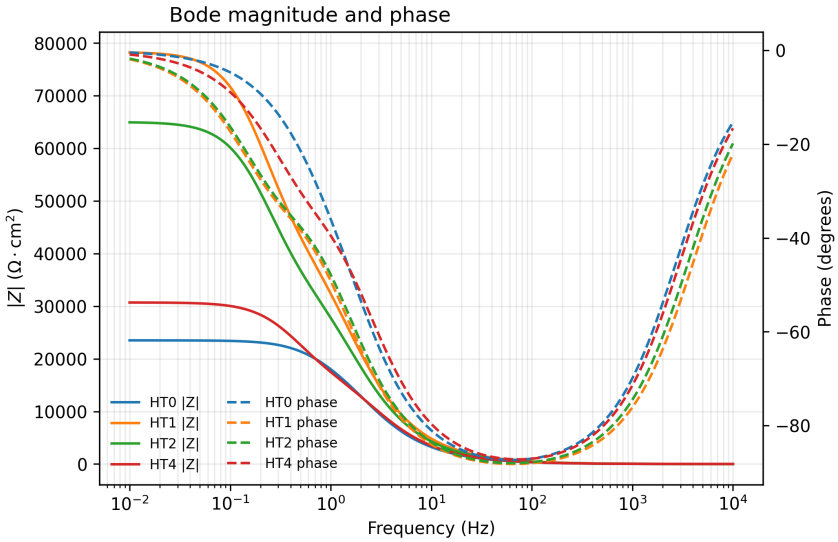

Figure 4: Bode magnitude and phase plots highlighting time-constant shifts with heat treatment.

The fitted parameters in Table 4 demonstrate a strong and systematic dependence on heat-treatment state. Solution resistance R_s remains essentially constant across conditions (∼12 $\Omega\,\mathrm{cm}^2$), indicating stable electrolyte conductivity and comparable cell geometry. In contrast, both R_{ct} and R_{ox} vary substantially with aging state. Moving from HT0 to HT1, R_{ct} increases from approximately 8 $\mathrm{k}\Omega\,\mathrm{cm}^2$ to ∼44–46 $\mathrm{k}\Omega\,\mathrm{cm}^2$, while R_{ox} increases from ∼15 $\mathrm{k}\Omega\,\mathrm{cm}^2$ to ∼32–33 $\mathrm{k}\Omega\,\mathrm{cm}^2$. Consequently, the polarization resistance R_p rises by more than a factor of three, reaching ∼75–78 $\mathrm{k}\Omega\,\mathrm{cm}^2$ for HT1. This behavior indicates that the peak-aged microstructure promotes both slower net charge transfer and a more resistive interfacial film.

As the microstructure transitions to over-aged states (HT2–HT4), the impedance-derived resistances decrease progressively. For HT2, R_{ct} and R_{ox} remain elevated relative to HT0 but are lower than HT1, and the combined R_p decreases to ∼61–65 $\mathrm{k}\Omega\,\mathrm{cm}^2$. The decline continues for HT3, where R_p falls to ∼45–47 $\mathrm{k}\Omega\,\mathrm{cm}^2$, and approaches near-baseline values by HT4 (∼27–31 $\mathrm{k}\Omega\,\mathrm{cm}^2$). The corresponding Bode plots show these trends as a reduction in low-frequency impedance magnitude and a shift in the phase-angle peak(s), reflecting changes in the characteristic timescales of film response and interfacial kinetics. The CPE exponents (n_{dl} and n_{ox}) remain within physically reasonable ranges (typically 0.77–0.92), with lower n_{ox} values in HT1 suggesting a more heterogeneous or distributed film response consistent with finely dispersed microstructural features and non-uniform film thickness at the microscale.

Taken together, the EIS results reveal a pronounced optimum in interfacial resistance at the peak-aged condition (HT1), followed by monotonic degradation with over-aging. This trend aligns with the microstructural descriptors: the finely dispersed, highly connected state (high κ) is associated with the largest R_{ct} and R_{ox}, whereas coarsening and reduced connectivity correlate with decreasing resistive contributions. These observations support the interpretation that the peak-

aged microstructure favors the development of a more resistive and stable surface film while also reducing the effective rate of net charge transfer under near-equilibrium conditions.

Table 4: EIS fit parameters for the adopted model. Values represent mean ± 95% confidence interval from equivalent circuit fitting.

Sample–Condition	R_s ($\Omega\,cm^2$)	R_{ct} ($k\Omega\,cm^2$)	R_{ox} ($k\Omega\,cm^2$)	n_{dl}	n_{ox}	R_p ($k\Omega\,cm^2$)
A1–HT0	12.8 ± 0.9	7.8 ± 0.6	14.7 ± 1.0	0.91 ± 0.02	0.84 ± 0.04	22.5 ± 1.2
A2–HT0	12.5 ± 0.8	8.2 ± 0.5	15.3 ± 1.1	0.92 ± 0.02	0.85 ± 0.03	23.5 ± 1.3
A1–HT1	11.9 ± 0.6	43.5 ± 2.1	31.8 ± 1.7	0.88 ± 0.02	0.77 ± 0.03	75.3 ± 2.8
A2–HT1	11.8 ± 0.6	45.7 ± 2.3	32.6 ± 1.8	0.89 ± 0.02	0.78 ± 0.02	78.3 ± 3.0
A1–HT2	12.2 ± 0.7	35.2 ± 1.8	25.4 ± 1.4	0.90 ± 0.01	0.79 ± 0.02	60.6 ± 2.3
A2–HT2	12.0 ± 0.7	38.1 ± 2.0	26.9 ± 1.5	0.89 ± 0.02	0.80 ± 0.02	65.0 ± 2.5
A1–HT3	12.3 ± 0.8	26.5 ± 1.4	18.2 ± 1.1	0.89 ± 0.02	0.80 ± 0.03	44.7 ± 1.9
A2–HT3	12.1 ± 0.7	28.4 ± 1.5	18.9 ± 1.2	0.90 ± 0.01	0.81 ± 0.02	47.3 ± 2.1
A1–HT4	12.7 ± 0.9	15.3 ± 1.0	12.1 ± 0.9	0.91 ± 0.02	0.83 ± 0.03	27.4 ± 1.4
A2–HT4	12.6 ± 0.8	17.2 ± 1.1	13.5 ± 1.0	0.92 ± 0.01	0.84 ± 0.03	30.7 ± 1.5

3.3 Polarization behavior and pitting susceptibility

Potentiodynamic polarization curves (Figure 5) provide complementary insight into corrosion kinetics, passive stability, and breakdown behavior. Across all conditions, the curves display an initial cathodic branch dominated by hydrogen evolution and oxygen reduction (depending on dissolved oxygen content), followed by an anodic branch where active dissolution transitions into a passive-like region and, at sufficiently positive potentials, breakdown consistent with localized attack. The extracted parameters (Table 5) show systematic improvements in corrosion performance for peak-aged conditions.

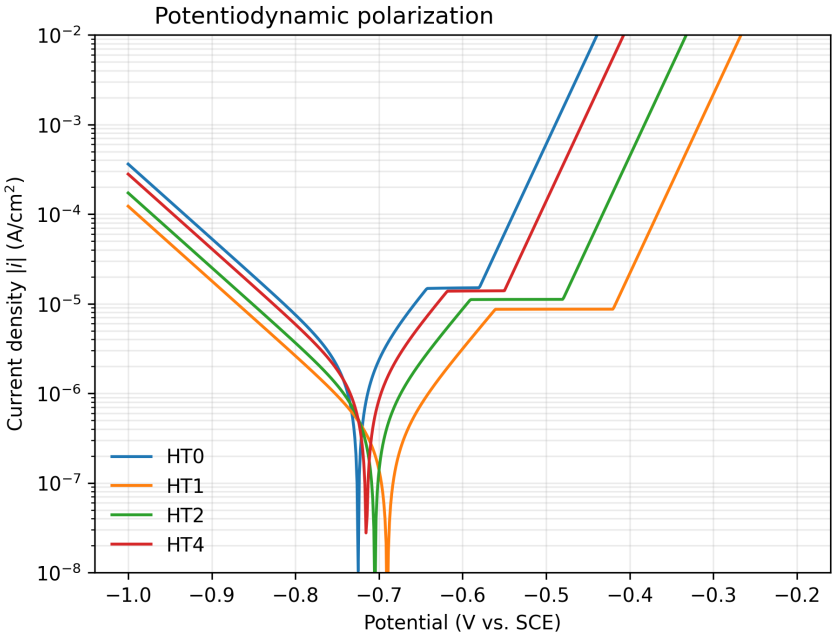

Figure 5: Potentiodynamic polarization curves for representative alloys and heat treatments.

From HT0 to HT1, the corrosion potential shifts in the noble direction (less negative E_{corr}), the corrosion current density decreases substantially, and the passive current drops, indicating both reduced uniform corrosion rate and improved passive behavior. For example, I_{corr} decreases from ∼1.8–1.9 µA cm^{-2} at HT0 to ∼0.32–0.35 µA cm^{-2} at HT1, representing an approximately five- to six-fold reduction. Simultaneously, the pitting potential becomes markedly less negative, shifting from around −0.58 to −0.42 V vs. SCE, consistent with increased resistance to passive film breakdown. These changes are consistent with the EIS-derived increases in both R_{ct} and R_{ox}, reinforcing the interpretation that peak aging promotes a more resistive interfacial response and delays the onset of localized instability.

As aging proceeds beyond HT1, the polarization metrics degrade gradually. Slight over-aging (HT2) yields intermediate values of I_{corr} and E_{pit} between HT1 and HT0, while further over-aging (HT3 and HT4) continues to reduce passive stability

and increase corrosion current. The recovery toward higher I_{corr} and lower E_{pit} at HT4 is consistent with coarsened second phases and reduced microstructural uniformity, which can re-establish local galvanic intensity and disrupt the continuity of protective films. The observed ordering across HT states therefore mirrors the impedance trends and provides an independent confirmation of a heat-treatment optimum in corrosion performance.

Table 5: Polarization parameters extracted from potentiodynamic curves. Values represent mean ± standard deviation (n=3).

Sample–Condition	E_{corr} (V vs. SCE)	I_{corr} (µA cm^{-2})	E_{pit} (V vs. SCE)	I_{pass} (µA cm^{-2})
A1–HT0	-0.730 ± 0.020	1.92 ± 0.15	-0.590 ± 0.012	16.1 ± 1.8
A2–HT0	-0.725 ± 0.015	1.85 ± 0.12	-0.580 ± 0.010	15.2 ± 1.5
A1–HT1	-0.695 ± 0.012	0.35 ± 0.05	-0.430 ± 0.018	9.2 ± 1.0
A2–HT1	-0.690 ± 0.010	0.32 ± 0.04	-0.420 ± 0.015	8.7 ± 0.8
A1–HT2	-0.710 ± 0.014	0.65 ± 0.07	-0.490 ± 0.016	11.8 ± 1.3
A2–HT2	-0.705 ± 0.013	0.60 ± 0.06	-0.480 ± 0.014	11.2 ± 1.1
A1–HT3	-0.710 ± 0.015	0.82 ± 0.09	-0.530 ± 0.015	12.8 ± 1.4
A2–HT3	-0.705 ± 0.012	0.78 ± 0.08	-0.520 ± 0.012	12.3 ± 1.2
A1–HT4	-0.720 ± 0.018	1.25 ± 0.11	-0.560 ± 0.013	14.5 ± 1.6
A2–HT4	-0.715 ± 0.016	1.18 ± 0.10	-0.550 ± 0.012	14.0 ± 1.5

3.4 Hydrogen evolution and anodic efficiency under discharge

Figure 6 reports hydrogen evolution rates at OCP and during galvanostatic discharge, providing a direct measure of parasitic reaction severity. Across both compositions, the peak-aged condition (HT1) exhibits the lowest HER, consistent with the highest impedance-derived resistances and the lowest corrosion current densities. This indicates that the microstructural state achieved at HT1 not only improves corrosion resistance under near-equilibrium electrochemical testing but also suppresses cathodic hydrogen evolution under practical operating conditions, which is essential for improving anode utilization.

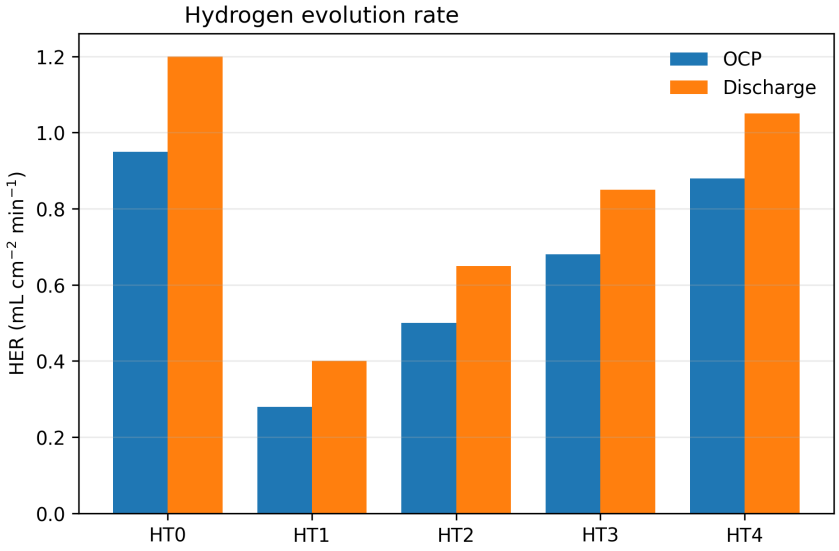

Figure 6: Hydrogen evolution rate (HER) at OCP and under discharge for selected conditions

The discharge-based utilization metrics in Table 6 further confirm this trend. In the as-quenched state (HT0), anodic efficiency is modest (approximately 59–60%), indicating substantial aluminum consumption through parasitic pathways. After peak aging (HT1), efficiency increases dramatically to approximately 92–95%, implying that the majority of consumed aluminum contributes to useful electrical charge rather than hydrogen generation and chemical corrosion. Slight over-aging (HT2) yields intermediate efficiencies (approximately 79–82%), while further over-aging (HT3) reduces efficiency to around 71%, and severe over-aging (HT4) returns efficiency toward near-baseline values (approximately 62%). The ordering of η_a across conditions is therefore consistent with both the EIS-derived R_p and the polarization-derived I_{corr}, establishing internal consistency across independent measurements.

Table 6: Mass loss, charge delivery, and anodic efficiency during discharge. Values represent mean ± standard deviation (n=3).

Sample–Condition	Δm (g)	Q_{useful} (C)	$Q_{\text{theoretical}}$ (C)	η_a (%)
A1–HT0	0.158 ± 0.009	890 ± 35	1510 ± 48	58.9 ± 3.0
A2–HT0	0.152 ± 0.008	875 ± 32	1450 ± 45	60.3 ± 2.8
A1–HT1	0.140 ± 0.007	1235 ± 42	1340 ± 41	92.2 ± 3.6
A2–HT1	0.138 ± 0.006	1250 ± 40	1320 ± 38	94.7 ± 3.5
A1–HT2	0.146 ± 0.008	1105 ± 38	1395 ± 44	79.2 ± 3.4
A2–HT2	0.144 ± 0.007	1120 ± 39	1375 ± 43	81.5 ± 3.5
A1–HT3	0.148 ± 0.008	995 ± 36	1410 ± 45	70.6 ± 3.2
A2–HT3	0.145 ± 0.007	980 ± 35	1385 ± 42	70.8 ± 3.1
A1–HT4	0.155 ± 0.009	920 ± 34	1480 ± 47	62.2 ± 3.1
A2–HT4	0.153 ± 0.008	905 ± 33	1460 ± 46	62.0 ± 3.0

Galvanostatic discharge curves in Figure 7 show corresponding improvements in operational stability. Peak-aged samples sustain a higher and more stable discharge plateau, with reduced voltage fluctuation attributable to suppressed bubble-induced polarization and more stable film behavior. In contrast, HT0 and HT4 conditions show earlier voltage decay and larger fluctuations, consistent with intensified hydrogen evolution and less protective interfacial films. The combined HER, mass-loss, and discharge evidence supports a unified interpretation: heat treatments that maximize passive-film resistance and stabilize interfacial kinetics simultaneously minimize hydrogen evolution and maximize anodic efficiency.

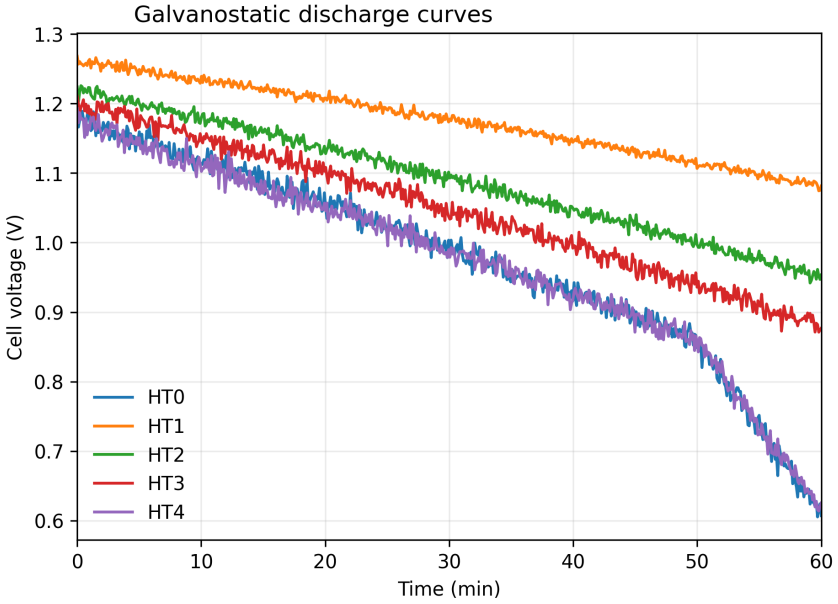

Figure 7: Galvanostatic discharge curves at fixed current density for representative samples/conditions

4. Discussion

The expanded results establish a consistent process–structure–electrochemistry–performance chain across the investigated conditions [5, 9, 11]. Heat treatment systematically modifies the morphology and connectivity of second-phase features (Table 3) [11], which in turn governs (i) the impedance-resolved partition between charge-transfer resistance R_{ct} and film resistance R_{ox} (Table 4) [10], (ii) polarization-derived corrosion kinetics and breakdown susceptibility (Table 5) [8], and (iii) parasitic hydrogen evolution and discharge-based anodic efficiency (Table 6) [7]. The central outcome is the emergence of a well-defined optimum at the peak-aged state (HT1), where the microstructure is highly refined and spatially pervasive, the interfacial film response is most resistive, and functional anode utilization is maximized.

The quantitative descriptors show that aging transforms the microstructure from a sparse coarse-constituent state (HT0: low f_{IM}, very large d_{IM}, low κ) into a finely dispersed high-connectivity state (HT1: higher f_{IM}, sub-micron d_{IM}, high κ), followed by progressive coarsening and loss of network continuity with over-aging (HT2–HT4: increasing d_{IM}, decreasing κ). While the absolute values of f_{IM}, d_{IM}, and κ depend on segmentation choices and imaging scale, their monotonic trends with aging provide a robust structural basis for interpreting electrochemical behavior [12]. Importantly, the microstructure

evolves in two distinct ways: (i) the density of phase boundaries and local heterogeneities increases strongly from HT0 to HT1 (fine dispersion), and (ii) the topological connectivity of second phases decreases again from HT1 to HT4 (coarsening and clustering). These two features are expected to influence alkaline corrosion differently, because fine dispersion can promote spatial uniformity of surface film formation, whereas high cathodic connectivity can amplify hydrogen evolution when electrochemically noble sites percolate.

The impedance results reveal that HT1 yields the largest R_{ct} and R_{ox} simultaneously, and therefore the largest polarization resistance R_p [9]. The increase in R_{ct} suggests that the net interfacial kinetics for charge transfer slow substantially in the peak-aged state [13]. In an alkaline environment, this net kinetic response reflects the superposition of anodic dissolution at Al-rich sites and cathodic reactions (notably hydrogen evolution) at electrochemically favorable regions [7]. A rise in R_{ct} can therefore be interpreted as an overall suppression of these charge-transfer processes, consistent with lower measured I_{corr} from polarization [8]. The concurrent rise in R_{ox} indicates that the passive/corrosion-product film becomes more resistive and/or less permeable to ionic transport, which is critical because film stability can regulate both anodic metal dissolution and the accessibility of cathodic sites [10].

A mechanistic explanation consistent with the microstructural metrics is that the refined HT1 microstructure promotes the development of a more continuous and mechanically stable surface film [10]. In multiphase Al alloys, coarse isolated intermetallics (HT0) tend to create strong local galvanic couples and steep local alkalinity gradients, driving non-uniform film growth and localized film rupture near particle–matrix boundaries. By contrast, a fine dispersion of second phases can reduce the characteristic length scale of galvanic cells, distributing local current more evenly and supporting a more uniform corrosion-product layer [12, 14]. Although κ is high in HT1, indicating a pervasive distribution, the key factor is not connectivity alone but the combination of high particle density with small d_{IM}, which can reduce "hot spots" that otherwise generate intense localized hydrogen evolution and localized dissolution. The lower n_{ox} values in HT1 further suggest a distributed film response, consistent with a film of varying thickness over a fine microstructure rather than a patchy film dominated by isolated pits [15].

From HT1 to HT4, both R_{ct} and R_{ox} decrease progressively, accompanied by increasing I_{corr} and reduced E_{pit} [6, 8]. This degradation aligns with microstructural coarsening (increasing d_{IM}) and reduced connectivity (κ), implying that the interfacial response becomes governed again by fewer, larger, and more spatially separated cathodic sites [11, 12]. Larger features intensify current localization at particle–matrix junctions and can generate higher local reaction rates per site. In alkaline media, this typically accelerates hydrogen evolution at cathodic regions, increases interfacial alkalinity near bubble nucleation sites, and destabilizes protective hydroxide/oxide films through repeated film rupture and re-precipitation. The observed reduction in R_{ox} is consistent with a film that is either thinner, more porous, or more frequently disrupted by localized attack and gas evolution [10]. At the same time, the reduced R_{ct} suggests that the net kinetics become faster, consistent with the increase in polarization-derived corrosion current [9].

The implication is that over-aging does not simply reduce mechanical strength or hardness (as in traditional precipitation systems), but directly undermines electrochemical stability by re-establishing a microstructure that supports localized galvanic coupling [16]. Even though the measured f_{IM} remains similar from HT1 through HT4, the topology (size and distribution) changes markedly, demonstrating that phase fraction alone is insufficient for predicting corrosion and anode utilization [11]. Instead, morphology and connectivity must be treated as primary state variables [12].

Polarization trends mirror the impedance results, strengthening confidence in the inferred mechanisms. The substantial reduction in I_{corr} at HT1 is consistent with the increase in R_p, while the shift of E_{pit} to less negative values indicates a more stable passive regime and delayed breakdown [8, 10]. The simultaneous reduction in passive current I_{pass} suggests a film that limits ionic transport and slows sustained dissolution in the passive region. Over-aging reverses these improvements, producing higher I_{corr} and lower E_{pit}, consistent with a more defective or discontinuous film response (lower R_{ox}) and enhanced localized attack [6,8]. The alignment of these independent methods supports the validity of separating film resistance and charge-transfer contributions in the impedance model and using these parameters as predictors of performance.

The hydrogen evolution and discharge results provide the most application-relevant confirmation of the process–structure–performance hypothesis. The dramatic increase in anodic efficiency from roughly 60% (HT0) to above 90% (HT1) indicates that the peak-aged condition not only improves electrochemical resistance metrics but also substantially suppresses parasitic pathways during operation [7, 14]. Because anodic efficiency incorporates both delivered charge and mass loss, it captures chemical corrosion and electrochemical side reactions in a single metric [5]. The HT1 condition reduces mass loss for a given delivered charge, implying that a larger fraction of aluminum consumption contributes to useful external current [14]. This is consistent with suppressed hydrogen evolution, since HER directly consumes electrons that would otherwise contribute to load current, and it promotes mechanical disruption of surface films via bubble formation [7].

In practical Al–air operation, hydrogen evolution can also increase apparent polarization through bubble coverage and mass-transfer blockage, causing voltage fluctuations and premature plateau decay. The more stable discharge plateaus

observed for HT1 are therefore consistent with reduced bubble-induced resistance and a more uniform, resilient film [5]. Conversely, the larger voltage fluctuations and earlier decay in HT0 and HT4 conditions are consistent with intensified HER and repeated film breakdown, which can create transient resistive layers followed by sudden exposure of fresh aluminum and renewed corrosion bursts.

At first glance, the peak-aged condition exhibits the highest connectivity metric κ, which might appear inconsistent with a purely galvanic interpretation where higher cathodic connectivity should worsen corrosion. The resolution is that κ alone does not determine galvanic severity; it must be interpreted together with the feature size d_{IM} and the spatial uniformity of the network [12]. In HT1, connectivity arises from a dense distribution of very fine features, which can produce many short-range galvanic interactions but reduce extreme localization and support uniform film formation [11]. In over-aged states, connectivity declines, but the remaining features are larger and more discrete, which increases the intensity of each localized cathodic site and promotes film rupture at fewer but more aggressive locations. Therefore, an improved predictor of parasitic behavior is not κ alone but a combined morphological index, for example κ/d_{IM} or a composite "galvanic localization parameter" that weights connectivity by particle size and spacing [12]. The observed optimum at HT1 suggests that fine-scale connectivity that promotes uniformity can be beneficial, whereas coarse-scale connectivity (or sparse large cathodes) is detrimental [11, 13].

The results provide practical guidance for optimizing multiphase aluminum anodes in concentrated alkaline electrolytes [14,15]. First, heat treatment can be used as a primary lever to tune intermetallic topology and thereby control film resistance and hydrogen evolution [11, 12]. Second, the best-performing state corresponds to a microstructure that promotes high film resistance (R_{ox}) while also increasing R_{ct}, indicating suppressed net interfacial kinetics. Third, over-aging should be avoided because coarsening reduces film integrity and increases parasitic reactions, even when the overall phase fraction remains similar. These insights motivate process maps that target a narrow window of aging conditions rather than monotonic trends with temperature/time [14].

From a modeling perspective, the strong empirical correspondence among R_{ox}, I_{corr}, HER, and η_a suggests that impedance-derived film resistance can serve as a rapid screening metric for anode candidates. If validated across broader compositions and current densities, R_{ox} (and its evolution under load) could be used to predict utilization without requiring long discharge experiments for every candidate condition [5, 14].

While the present results provide a coherent framework, several limitations should be addressed in future work [14]. The impedance parameters were extracted at OCP, whereas anodes operate under significant anodic polarization during discharge; extending EIS to in-situ measurements under galvanostatic bias would strengthen causality between film resistance and operational efficiency. Additionally, direct characterization of the surface film chemistry and thickness (e.g., XPS, Raman, cross-sectional SEM/TEM) would clarify whether the increase in R_{ox} reflects thicker films, less porous films, different hydroxide/oxide composition, or changes in defect density. Finally, since the electrochemical environment evolves with dissolved oxygen, temperature, and electrolyte concentration, a sensitivity study over these parameters would broaden applicability to realistic Al–air battery conditions [14].

5. Conclusion

The results collectively confirm a strong and internally consistent process–structure–electrochemistry–performance linkage for Al–Co–Mn anodes in concentrated alkaline electrolyte. Heat treatment is shown to be an effective primary lever for controlling second-phase topology, and this microstructural control directly governs the partitioning of interfacial response into charge-transfer resistance and film resistance, the corrosion and breakdown signatures observed in polarization, and—most critically—the magnitude of parasitic hydrogen evolution and the achievable discharge-based anodic efficiency. Across all metrics, the peak-aged condition (HT1) emerges as the optimal state, combining a highly refined and spatially pervasive dispersion of second phases with the most resistive and stable interfacial film response, yielding the lowest corrosion current, the most favorable breakdown behavior, the most suppressed hydrogen evolution, and the highest utilization of aluminum under load. Over-aging systematically erodes these gains: coarsening and reduced network continuity shift the system back toward localized galvanic coupling, more frequent film disruption, reduced film resistance, accelerated corrosion kinetics, intensified hydrogen evolution, and diminished discharge stability and efficiency. These findings demonstrate that phase fraction alone is insufficient for predicting anode performance; instead, morphology and connectivity must be treated as primary state variables that determine whether microstructural refinement promotes uniform film formation or, conversely, enables aggressive localized cathodic activity. Practically, the work indicates that maximizing Al–air anode utilization requires targeting a narrow heat-treatment window that produces fine-scale, well-distributed second phases capable of supporting a high-resistance, resilient corrosion-product film while suppressing net interfacial kinetics. Finally, the observed correspondence between impedance-derived film resistance and functional utilization supports the use of EIS-based film met-

rics as rapid screening parameters for anode optimization, while motivating future validation under in-situ biased EIS and direct film-chemistry characterization to strengthen mechanistic causality and broaden applicability to realistic operating envelopes.

References

[1] Bruce, P. G., Freunberger, S. A., Hardwick, L. J., & Tarascon, J. M. (2012). Li–O2 and Li–S batteries with high energy storage. *Nature Materials, 11*(1), 19-29.

[2] Girishkumar, G., McCloskey, B., Luntz, A. C., Swanson, S., & Wilcke, W. (2010). Lithium-air battery: promise and challenges. *The Journal of Physical Chemistry Letters, 1*(14), 2193-2203.

[3] Christensen, J., Albertus, P., Sanchez-Carrera, R. S., Lohmann, T., Kozinsky, B., Liedtke, R., ... & Kojic, A. (2011). A critical review of Li/air batteries. *Journal of the Electrochemical Society, 159*(2), R1.

[4] Garcia-Araez, N., & Novák, P. (2013). Critical aspects in the development of lithium–air batteries. *Journal of Solid State Electrochemistry, 17*(7), 1793-1807.

[5] Newman, J., & Balsara, N. P. (2021). *Electrochemical Systems*. John Wiley & Sons.

[6] Zhang, J., Klasky, M., & Letellier, B. C. (2009). The aluminum chemistry and corrosion in alkaline solutions. *Journal of Nuclear Materials, 384*(2), 175-189.

[7] Doche, M. L., Rameau, J. J., Durand, R., & Novel-Cattin, F. (1999). Electrochemical behaviour of aluminium in concentrated NaOH solutions. *Corrosion Science, 41*(4), 805-826.

[8] Frankel, G. S. (1998). Pitting corrosion of metals: a review of the critical factors. *Journal of the Electrochemical Society, 145*(6), 2186.

[9] Mansfeld, F. (1990). Electrochemical impedance spectroscopy (EIS) as a new tool for investigating methods of corrosion protection. *Electrochimica Acta, 35*(10), 1533-1544.

[10] Macdonald, D. D. (1992). The point defect model for the passive state. *Journal of the Electrochemical Society, 139*(12), 3434.

[11] Birbilis, N., & Buchheit, R. G. (2005). Electrochemical characteristics of intermetallic phases in aluminum alloys: an experimental survey and discussion. *Journal of the Electrochemical Society, 152*(4), B140.

[12] Brunner, J. G., Birbilis, N., Ralston, K. D., & Virtanen, S. (2012). Impact of ultrafine-grained microstructure on the corrosion of aluminium alloy AA2024. *Corrosion Science, 57*, 209-214.

[13] Liu, Y., Wu, Z., Qin, Z., Liu, Y., & Hu, W. (2024). Recent progress in inhibition of hydrogen evolution reaction in alkaline Al-air batteries. *National Science Open, 3*(6), 20240037.

[14] Wu, S., Zhang, Q., Ma, J., Sun, D., Tang, Y., & Wang, H. J. M. T. E. (2020). Interfacial design of Al electrode for efficient aluminum-air batteries: issues and advances. *Materials Today Energy, 18*, 100499.

[15] Song, G., & Atrens, A. (2003). Understanding magnesium corrosion—a framework for improved alloy performance. *Advanced Engineering Materials, 5*(12), 837-858.

[16] Zhao, R., He, P., Yu, F., Yang, J., Sun, Z., & Hu, W. (2023). Performance improvement for aluminum-air battery by using alloying anodes prepared from commercially pure aluminum. *Journal of Energy Storage, 73*, 108985.